Computational and Structural Biotechnology Journal 21 (2023) 224–237

COMPUTATIONAL AND STRUCTURAL BIOTECHNOLOGY JOURNAL

journal homepage: www.elsevier.com/locate/csbj

A deep learning-based tool for the automated detection and analysis of caveolae in transmission electron microscopy images

María C.M. Aboy-Pardal [a,*], Daniel Jimenez-Carretero [b], Sara Terrés-Domínguez [a], Dácil M. Pavón [a], Laura Sotodosos-Alonso [a], Víctor Jiménez-Jiménez [a], Fátima Sánchez-Cabo [b], Miguel A. Del Pozo [a,*]

[a] Mechanoadaptation and Caveolae Biology lab, Cell and Developmental Biology Area. Centro Nacional de Investigaciones Cardiovasculares (CNIC), 28029 Madrid, Spain
[b] Bioinformatics Unit, Centro Nacional de Investigaciones Cardiovasculares (CNIC), 28029 Madrid, Spain

ARTICLE INFO

Article history:
Received 3 August 2022
Received in revised form 29 November 2022
Accepted 29 November 2022
Available online 5 December 2022

Keywords:
Caveolae
TEM
Deep learning

ABSTRACT

Caveolae are nanoscopic and mechanosensitive invaginations of the plasma membrane, essential for adipocyte biology. Transmission electron microscopy (TEM) offers the highest resolution for caveolae visualization, but provides complicated images that are difficult to classify or segment using traditional automated algorithms such as threshold-based methods. As a result, the time-consuming tasks of localization and quantification of caveolae are currently performed manually. We used the Keras library in R to train a convolutional neural network with a total of 36,000 TEM image crops obtained from adipocytes previously annotated manually by an expert. The resulting model can differentiate caveolae from non-caveolae regions with a 97.44% accuracy. The predictions of this model are further processed to obtain caveolae central coordinate detection and cytoplasm boundary delimitation. The model correctly finds negligible caveolae predictions in images from caveolae depleted Cav1$^{-/-}$ adipocytes. In large reconstructions of adipocyte sections, model and human performances are comparable. We thus provide a new tool for accurate caveolae automated analysis that could speed up and assist in the characterization of the cellular mechanical response.

1. Introduction

Caveolae are plasma membrane (PM) invaginations of 50–100 nm in diameter [1,2] particularly abundant in adipocytes, fibroblasts and endothelial cells. Caveolar structures constitute mechanosensitive platforms that flatten upon PM tension increase to protect cell integrity and transduce mechanical information from the cell surface into downstream signals [3–8].

Caveolin-1 (Cav1) protein is an essential component for caveolae formation, and Cav1$^{-/-}$ cells lack caveolae. Cav1 depletion or mutation has been linked to lipodystrophy syndromes in humans and reduced fat depots in mice [9–14]. Mutations in Cavin-1 (also called PTRF), another essential caveolar component, have also been linked to lipodystrophy [15–23], evidencing the importance of the caveolar structure for adipocyte biology. Thus, caveolar quantification often constitutes a significant step in the characterization of Cav1 and Cavin-1 mutants.

Visualization of nanoscopic caveolar structures requires high-resolution microscopy techniques. Super-resolution microscopy offers numerous advantages for caveolae analysis, including straightforward sample processing, the possibility of imaging living cells and a reasonable throughput. This technique also involves the use of fluorescent labels, enabling the study of different caveolar protein components, their spatial localization and interaction. Several approaches based on machine learning have been recently developed for the analysis of caveolar structures visualized by super-resolution microscopy [24–28]. However, the highest resolution for direct and definitive caveolae visualization is provided by Transmission Electron Microscopy (TEM). In TEM images, caveolae may appear as single-pits connected to the cell surface, internalized vesicles (cavicles), or organized in clustered structures (rosettes). These different caveolae categories have been associated with differential mechanical sensitivity, with a predominance of internalized or clustered caveolae in low-tension conditions [7,29–33]. Caveolae structure can thus provide information on the mechanical state of the cell.

The complexity of TEM images and the absence of fluorescent labels hampers the use of traditional, threshold-based algorithms

* Corresponding authors.
E-mail addresses: mcmaboy@outlook.es (M.C.M. Aboy-Pardal), madelpozo@cnic.es (Miguel A. Del Pozo).

https://doi.org/10.1016/j.csbj.2022.11.062

for automated caveolae analysis. Here, we present a deep-learning based approach for caveolae quantification and classification in TEM images. The tool was trained to recognize caveolae and is able to delimit the cytosolic boundaries with the extracellular matrix and the lipid droplet. The performance of the tool is comparable to manual quantification in reconstructed sections of adipocytes, and the amount of caveolar detections in $Cav1^{-/-}$ adipocytes is negligible. This tool has a clear potential to enable efficient and effortless caveolae detection in TEM images, allowing for thorough cellular mechanical characterization.

2. Materials and methods

2.1. Sample preparation

Epididymal adipose tissue was extracted from eight 38–50 weeks-old C57BL/6 mice fed with LabDiet 5 K67 - JL Rat & Mouse/Auto 6F. For ultrastructure imaging, epididymal adipose depots were immersed immediately after extraction in fixative solution: 2 % glutaraldehyde (G011 TAAB), 2 % formaldehyde (28908, Thermo) in phosphate buffer 0.1 M, pH 7.4 and minced in small pieces to favor surface contact. Samples were fixed overnight, washed and treated with osmium tetraoxide 1 % in water, followed by in block contrast with 0.5 % uranyl in water and then dehydrated with increasing ethanol concentrations (30, 50, 70, 95, 100 %). Finally, samples were acetone washed and included in epoxy resin Durcupan. Ultramicrotomy sections were performed with a thickness of 60 nm and then placed in cupper grids and stained with uranil acetate (2 %) and Reynolds lead.

3T3-L1 cells were plated on permanox plastic chambers (ThermoFisher 177445PK) and maintained at 37 °C 5 % CO_2 with culture media DMEM (Gibco 11995073) 10 % FBS (HyClone SV30160.03), penicillin/streptamicin (Gibco L1953096). Adipogenic differentiation was performed with the following adipogenic factors added to culture media: 5 µg/ml insulin in 3 mM HCl (Sigma I5500); 25 µg/ml IBMX (Sigma I5879); 1 µg/ml dexamethasone (Sigma D4902); 0,4415 µg/ml troglitazone (Calbiochem 648469). After 48 h, media was replaced with new differentiation media including only insulin and troglitazone. From this point, media was changed every other day adding only insulin. Cells were fixed at 8 days post differentiation with fixative solution: 2 % glutaraldehyde (G011 TAAB), 2 % formaldehyde (28908, Thermo) in phosphate buffer 0.1 M, pH 7.4. Cells were left for 1 h in fixative solution and then washed three times in phosphate buffer 0.1 M, pH 7.4. They were then treated with osmium tetraoxide 1 % in water for 1 h, washed and contrasted with 0.5 % uranyl acetate. Chamber wells were removed and dehydration was performed with increasing ethanol concentrations (30, 50, 70, 95, 100 %) followed by inclusion in Epon resin. Ultramicrotomy sections were performed with a thickness of 60 nm and then placed in cupper grids and stained with uranil acetate (2 %) and Reynolds lead.

Mouse aorta samples were processed similarly to adipose tissue, but fixed instead in 0.1 M cacodylate buffer, pH 7.4 containing 2.5 % glutaraldehyde, 1 mg/ml ruthenium red.

Human dermal skin fibroblasts were treated for 10 min with a 1/10 dilution of DMEM to obtain 30 mOsm or with DMEM as a control. They were then fixed in 0.1 M cacodylate buffer, pH 7.4 containing 2.5 % glutaraldehyde, 1 mg/ml ruthenium red, and then post-fixed in 1 % osmium tetroxide, 1 mg/ml ruthenium red, followed by treatment with 2 % uranyl acetate. The samples were dehydrated, embedded in LX112 Epon resin, sectioned and stained.

All animal experiments were approved by CNIC and Universidad Autónoma de Madrid (UAM) Ethics Committees and by the competent authorities (Comunidad de Madrid, PROEX 051/16) in compliance with relevant regulations for research animal welfare.

2.2. Imaging, annotation and datasets

1024x1024 $pixel^2$ TEM images with pixel size 1.478 nm were obtained in a JEOL JEM1010 (100 kV) equipped with a digital camera Gatan Orius 200 SC with a magnification of 60000x. Three different caveolae experts evaluated 5018 adipose tissue TEM images and located caveolae central coordinates using the Fiji [34] Cell Counter plugin [35]. High classification agreement among the three experts was confirmed and then the cells to which these images belonged were distributed among the three experts at random so each image was analyzed once. At the moment of caveolae localization, the experts further classified caveolae in three categories: single-pits (typical caveolar individual invaginations connected to the cell surface), rosettes (caveolar clusters), and cavicles (invaginated caveolae detached from the cell surface). One of the experts used the multipoint tool of Fiji to locate sparse coordinates of lipid droplet (LD), extracellular matrix (ECM) and cytosol in the same adipose tissue images, and mitochondria, endoplasmic reticulum (ER) and endosomes in 3883 images of *in vitro* differentiated 3T3-L1 adipocytes. 100x100 $pixel^2$ (148x148 nm^2) crops centred at the coordinates located by the experts were automatically extracted with an ImageJ macro. One of the experts finally assessed all the crops to confirm correct annotation and discarded those that were not properly centred and where caveolae were not complete. Annotated image crops from all 9 categories (Fig. 1a) were randomly assigned to the training, validation and test set. The training set contained 3000 image crops of each category, while the validation and test sets both contained 500 image crops for each category. In total, 27,000 training and 4500 validation crops were used as input in the training process of a multiclass (9 categories) classification model. Input crops were loaded as greyscale and rescaled to values between 0 and 1. Data augmentation was applied to the training set, with a 40° random rotation, 20 % random horizontal shift, random shear transformations, 20 % random zoom and random horizontal flip. Data augmentation was intended to increase the generalization capability of the tool in caveolae TEM images of different orientations and magnifications.

Mouse aorta sections were imaged similarly to adipose tissue. Human dermal skin fibroblasts were examined at 80 kV with a JEOL JEM-1010 equipped with TVIPS F416 camera.

2.3. Learning architectures and downstream processing

2.3.1. CNN for cell structure classification

Using the Keras library (v 2.2.5) with the Tensorflow backend (v 2.2.0) in RStudio (1.1.463, R version 3.4.4), we implemented a convolutional neural network (TEMCell-CNN) with the architecture depicted in Fig. 1b, to perform classification of TEM image crops on 9 cellular structures. The network takes 100x100 $pixel^2$ image crops as input and has five hidden convolutional layers (of 32, 64, 64, 128 and 128 neurons). All convolutional layers use a 3x3 kernel and ReLU as activation function, followed by 2x2 max pooling layers. Outputs are flattened before undergoing a 0.5 dropout rate and are fed into a densely connected layer of 512 units. The output layer uses a softmax function returning a size-9 vector of probability scores, each corresponding to a different class and all adding up to 1. The class with the highest probability is considered as the predicted class. The network was trained for 400 epochs with a callback for early stopping when the validation accuracy did not improve during 20 epochs. Adam optimizer was used with learning rate 0.001 and categorical crossentropy as loss function. All the parameters were tested empirically and selected to maximize accuracy and avoid overfitting. In short, we first set up a model with a large number of layers. Layers were removed to reduce overfitting until the accuracy was affected; then dropout

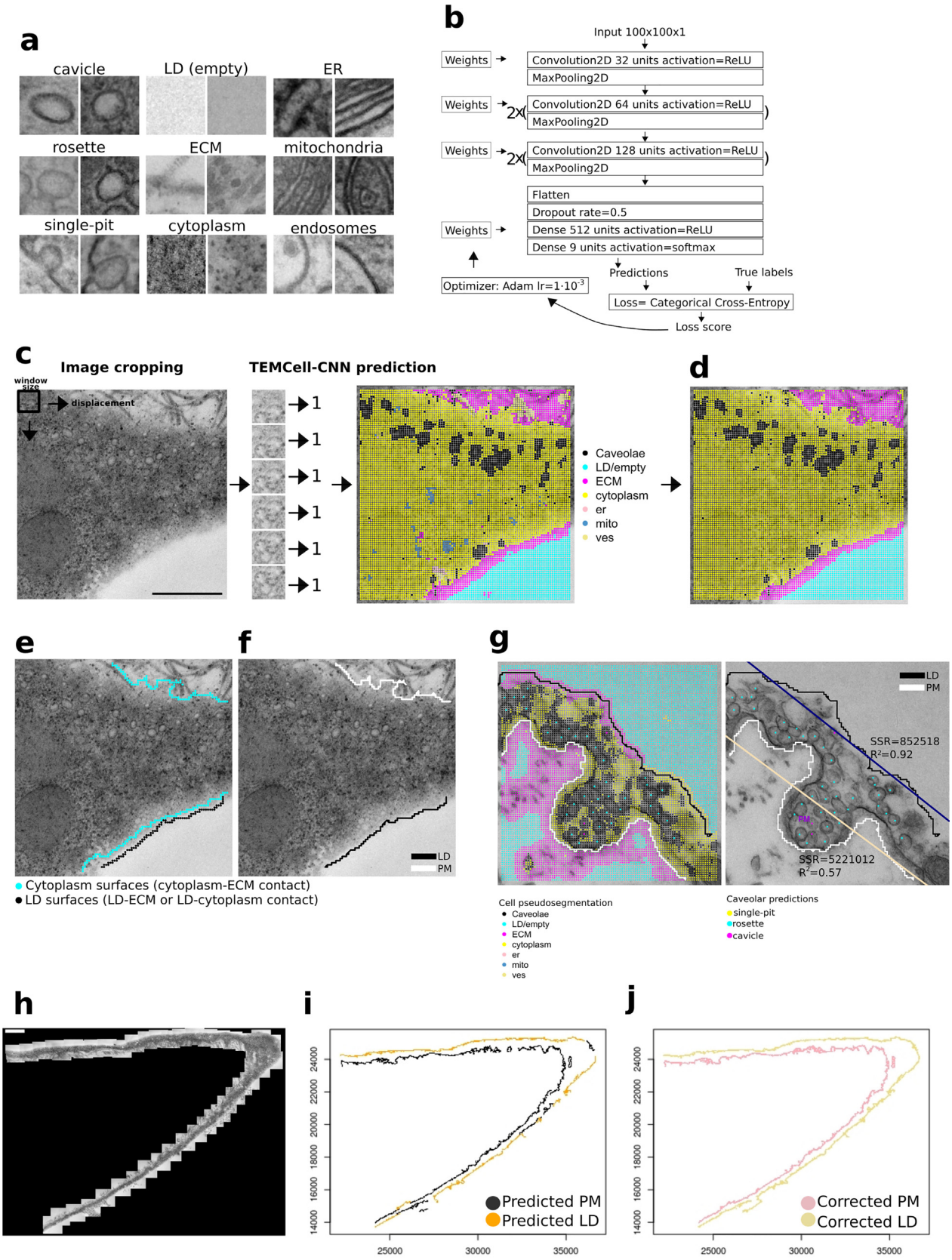

Fig. 1. Implementation of two CNNs for the classification of cellular and caveolar structures. A: Examples of image crops used in the training set. B: Architecture of TEMCell-CNN. C: Schematic representation of the scan process with TEMCell-CNN prediction on successive crops from an image and resulting pseudo-segmentation. D: Reassignment of small isolated areas with prediction errors to the surrounding predominant class to improve pseudo-segmentation consistency. E: Delimitation of cytoplasm surfaces by contact with ECM or LD. F: Classification of cytoplasm surfaces as PM or LD based on surface intricacy and classification of contact areas. G: Example of ECM containing empty areas and PM and LD classification based on intricacy. H: Manual stitching of an adipocyte section. I: Organization of PM and LD predictions obtained from individual tiles, and localized in space based on tile coordinates provided by manual stitching. J: Connection of surface segments by proximity and correction of PM and LD predictions based on the predominant type among the connected surface components. Scale bar: 0.5 μm in C; scale bar 1.5 μm in H.

was added until we found no overfitting. We varied the learning rate until we found a range where the network was able to learn (between $5{\cdot}10^{-5}$ and $5{\cdot}10^{-2}$), and then we completed the training with several values within that range and selected the one that provided the maximum accuracy.

A second model (TEMCav-CNN) was created to classify image crops exclusively on the three caveolar categories. The network architecture was similar to that of TEMCell-CNN, except that the output layer was composed of only three units for the three-class classification (single-pit, cavicle, and rosette), and the RMSProp optimizer was used with a learning rate of $5{\cdot}10^{-4}$.

2.3.2. Image pseudo-segmentation with TEMCell-CNN scan

2.3.2.1. Scan process. Although TEMCell-CNN model performs classification of image crops, a pseudo-segmentation of whole TEM images can be performed by using the model to scan through the image, classifying image crops at different discrete grid-like positions. Using a sliding-window approach (with a predefined, user-modifiable, window size and displacement), image crops are extracted and classified with TEMCell-CNN (Fig. 1c). If the user does not define the sliding-window parameters, the tool is able to provide a recommended sliding window and displacement based on image scale and typical caveolae diameter. Since the network was trained with 100x100 pixel^2 crops, if a different sliding-window size is selected, crops are reshaped before entering the network. Model predictions are assigned to the central coordinate of each crop, providing pseudo-segmentation of cell regions (Fig. 1c): not only predictions for cellular structures, but information about the spatial location within the image. User-defined windows size and displacement parameters allow to control the density of the grid and, therefore, the pseudo-segmentation obtained.

A knowledge-based refinement of predictions was later applied to increase pseudo-segmentation spatial consistency. Most classification errors involved small and isolated areas with spurious class predictions, so they are detected and reclassified to the predominant surrounding type (Fig. 1d). In order to do this, the tool automatically selects an organelle prediction (mitochondria, ER, endosome, LD) and associates it with the predictions of the same class that are within a distance equal to sliding window displacement. Then the process is repeated recursively with all the associated predictions, until no more are found within the displacement distance. This defines a class consistent patch with spatial contiguity. If the patch is below a certain threshold (5x average caveolae area for mitochondria, 3x average caveolae area for ER and endosomes, 10x for LD), it is assumed erroneous. In this case, the patch is reassigned to the class that is predominant among the coordinates in its immediate vicinity (i.e., within a distance equal to sliding window displacement, cytoplasm in the case of Fig. 1c-d). If the predominant class in the vicinity is caveolae, then it is reassigned to the cytoplasm class to avoid false positive caveolae predictions.

Finally, predictions of caveolar structures (single-pit, rosette and cavicle) were merged in a single caveolae category for further processing. Caveolar probability ($P_{caveolae}$) was calculated as $P_{single\text{-}pit} + P_{rosette} + P_{cavicle}$ and instances where $P_{caveolae}$ was higher than the prediction probability or any other category, were reassigned to the new caveolae category.

2.3.2.2. Cytoplasm-surface delimitation. Coordinates of cytoplasm-ECM and cytoplasm-LD contact are found based on pseudo-segmentation of ECM, LD, and cytoplasm classes (Fig. 1e). Cytoplasm-ECM contact surfaces would in principle correspond to PM, while cytoplasm-LD contact regions would be classified as LD surface. However, cytoplasmic areas in contact with the LD are frequently classified as ECM, which could lead to errors (Fig. 1d). Similarly, empty regions in ECM can be indistinguishable from LD (Fig. 1g). Interestingly, PM profile tends to show a higher intricacy, as compared to flatter LD surfaces (Fig. 1g). If cytoplasmic surface coordinates are fitted to a regression line, a R^2 and sum of squared residuals (SSR) can be obtained as measurement of surface intricacy, since more intricate surface would show a bad fitting to the regression line. In cases where a cytoplasmic surface is in contact with regions classified as ECM and LD, the surface with a value of SSR > $1{\cdot}10^6$ is classified as PM (Fig. 1g).

Surface classification in individual images can lead to errors, arising, for example, from the existence of precipitates in the LD area that can lead to wrong surface delimitation and misclassifications (Supp. Fig. 1a). A global correction and refinement of classification of cytoplasm surfaces can be performed when a series of overlapping TEM image tiles for a cell section are available (Fig. 1h). The tool can analyse the tiles individually and later use global coordinates for each tile to organize and join surface segments of PM and LD predictions (Fig. 1h). Surface segments are joined by order of proximity, with a maximum of two connections per segment, and avoiding connections through cytoplasmic predictions. Segment surface predictions (PM and LD) are corrected based on the predominant prediction of the connected surface components (Fig. 1i-j), resulting on a globally consistent determination of PM and LD boundaries.

2.3.3. Accurate classification of caveolar structures

To provide caveolar structure recognition with further robustness and consistency, the algorithm automatically corrects and further analyses grid-like predictions with information from the surrounding spatial context. The objective is to better detect central positions of caveolae and improve their classification into the three categories of caveolar structures.

2.3.3.1. Central caveolae coordinate detection. Coordinates with caveolar predictions are classified in *isolated*, *border*, or *inner* depending on their number of caveolar coordinate neighbours (Fig. 2a-c). Isolated caveolar predictions are assumed errors and removed. Border caveolar predictions that are not in contact with inner caveolar predictions are also removed for caveolar region smoothing (Fig. 2c-d). Resulting caveolae predictions are then aggregated in class-consistent groups of spatial continuity (Fig. 2e). Because caveolae area ranges are known from the literature, and the number of caveolar predictions in a group is proportional to its size, some are expected to contain a single caveolae due to their size (Fig. 2f). In those cases where group size is consistent with both big individual caveolae and small caveolae duplets, the decision is taken based on circularity. Central coordinates for individual caveolae can then be easily calculated by averaging x,y coordinates (Fig. 2g). Average caveolae area in the image is calculated from groups whose size and circularity are compatible with individual caveolae. If no individual caveolae are found in the image, an average value based on reported average caveolae area is used instead for further processing.

Due to their size, some groups are expected to contain several caveolae. To find their multiple central caveolar coordinates in these cases, k-means-based cluster analysis is performed. Based on group size and the average caveolae area previously calculated for the image, an estimated value for the k parameter (number of caveolae) is assigned based on the formula:

$$k = round\left(0.44 + 0.66{\cdot}^{n_g}/\bar{A}\right)$$

Where n_g refers to group size and $\bar{A}$ to average caveolar area in the image. This formula was empirically determined by establish-

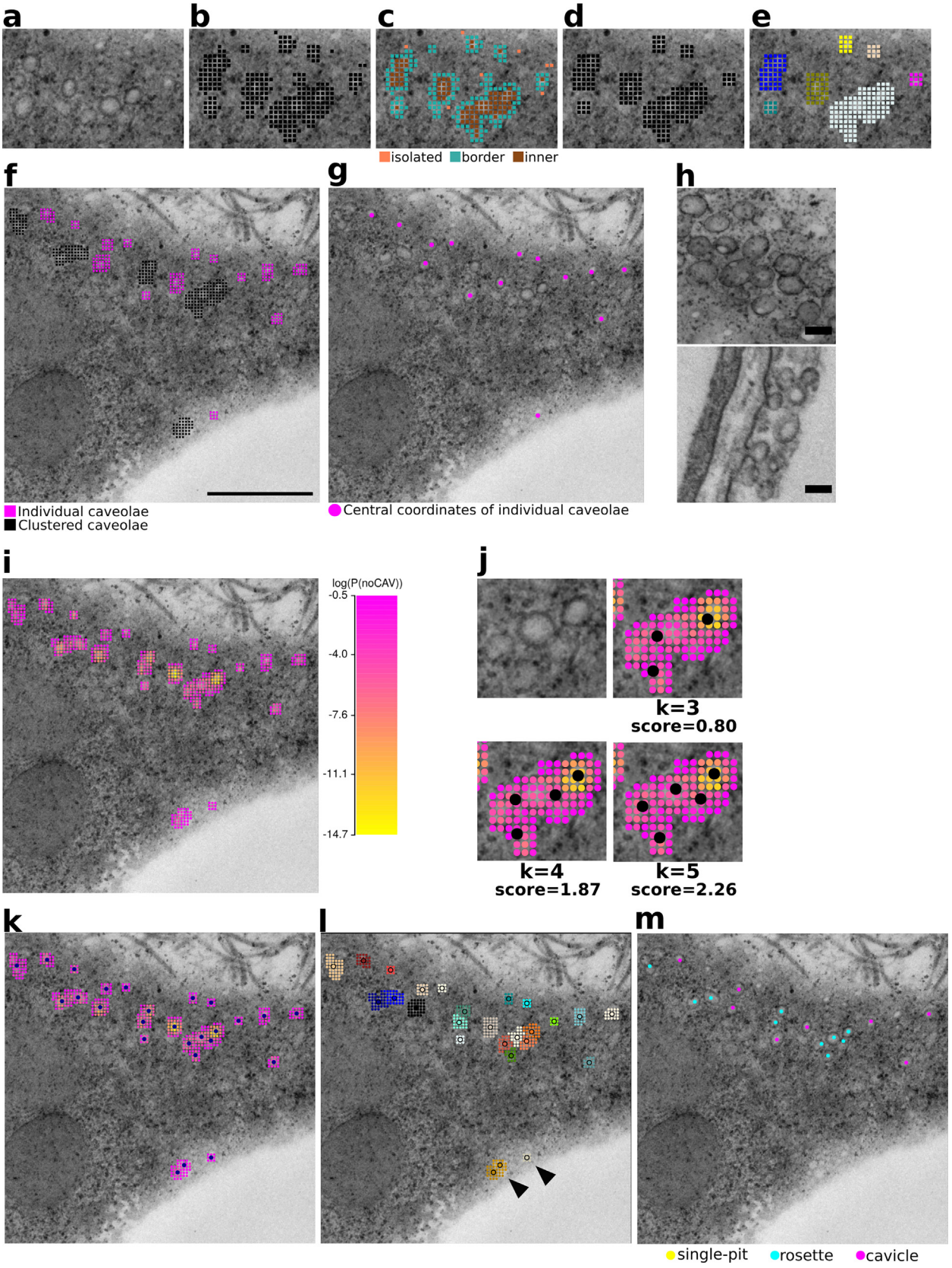

Fig. 2. Postprocessing of caveolar predictions obtained from TEMCell-CNN. A-E: The tool scans through TEM images (A) and TEMCell-CNN produces caveolar predictions (B) that are classified as isolated, border and inner (C) depending on their number of neighbours; coordinates that are not classified as inner, or that are not in direct contact with them, are then discarded for caveolar region smoothing (D). Caveolar predictions are finally grouped by spatial continuity (E). F: Finding of isolated caveolae (magenta) and multicaveolar groups (black) based on group area and circularity. G: Central caveolae finding in groups of isolated caveolae. H: Examples of caveolae in TEM images, evidencing their circular shape, and a low size variability in the same image. Scale bar: 100 nm. I: Caveolar prediction probabilities. J: Representative example of caveolar centres obtained from sequential implementations of the k-means algorithm and their respective scores. K: Final caveolae centre selection. l: Final clustering of caveolar predictions, providing a pseudo-segmentation for individual caveolae. M: Final caveolae classification by TEMCav-CNN. Scale bar in F: 0.5 μm; scale bar in H, 100 nm.

ing a correlation between the real number of caveolae in rosettes of some example images and the quotient between group size and estimated caveolae area.

Because caveolar area in the image presents some variability (Fig. 2h), *k+1* and *k-1* values are also considered. For each of the three options (k-1, k, k+1), the clustering approach based on k-means algorithm is run 10 times, providing a total of 30 sets of potential cluster centres (due to the stochastic component of the algorithm). These repetitive runs of the k-means algorithm are performed with the intention of finding an optimal solution.

Because the CNNs were trained with centred caveolae images, prediction probabilities tend to be higher at caveolae centres. Thus, cluster centres should ideally fall close to coordinates with high prediction probability (Fig. 2i). To achieve this, each of the 30 k-means implementations is run twice: after the first run of k-means on 2D coordinates, the obtained centres are used to initiate a second k-means that weights each point proportionally to its caveolar prediction probability (round(-log(1-$P_{caveolae}$)) times). This process intends to increase the probability of cluster centres falling near a real caveolae centre (Supp. Fig. 1b).

To decide the optimal solution among the resulting 30 sets of centres, every set of centres (and corresponding clusters) is provided with a score composed of five components:

Score = circularity – size variability + certainty – distance to border + centre colour intensity.

1- Circularity: caveolae tend to be highly circular (Fig. 2h), and thus circular clusters are favoured. For each cluster c in k, circularity is defined for every cluster as $\frac{n_c}{(b_c)^2}$, where n_c equals the number of points assigned to cluster c, and b_c equals the number of cluster points classified as border (Fig. 2c). The median of the circularity of the k clusters is then obtained for each iteration of the k-means.
2- Size variability: caveolae size may vary significantly in different cells, but caveolae in the same image tend to have very similar area (Fig. 2h). Thus, clusters with caveolae of similar size are favoured. Size variability is defined as $\sqrt{\frac{\sum_{c=1}^{k}(n_c-\bar{n})^2}{k-1}}$, where k equals total number of clusters; n_c equals size of cluster c, and $\bar{n}$ is the average size for the k clusters.
3- Certainty: because the CNN was trained with centred caveolae images, prediction probabilities tend to be higher at caveolae centres. Thus, centres falling close to coordinates with high prediction probability are favoured (Fig. 2i, j). To obtain the certainty parameter for a cluster, we first obtain the prediction probability of all m caveolar predictions of the group within a distance of (2·displacement) pixels to the cluster centre. Certainty is then obtained with the expression: $\sum_{i=1}^{m} -\log(1-P(caveolae)_i)$ where m is the number of caveolar predictions within a 2·displacement distance of the cluster centre, and $P(caveolae)_i$ is the probability of every caveolar prediction. Median cluster certainty for the k clusters of a group is then obtained.
4- Distance to border: centres falling close to caveolar predictions classified as *border* are penalized (Fig. 2c). This parameter is defined as $\frac{\sum_{c=1}^{k} b_{ic}}{k}$, where b_{ic} is the number of border caveolae predictions within a (short) distance of displacement + 1 pixels to the centre of cluster c and k is the number of clusters.
5- Colour intensity: most caveolae tend to be lighter in the centre in TEM images (Fig. 2h). Thus, centres falling in dark regions are penalized. For every cluster, a 148x148 nm^2 matrix M is obtained as a subset of the whole image matrix, centred in the cluster centre coordinates. A distance matrix D is obtained with the distance of every element of M to the cluster centre. The colour intensities in M are then weighted by their distances to the centre obtained in D: $\sum_{i=1}^{100}\sum_{j=1}^{100}\frac{m_{ij}}{0.1+2\cdot d_{ij}}$, where m_{ij} refers an element of the ith row and jth column of M and d_{ij} refers to an element of the ith row and jth column of D. Median colour intensity for the k clusters of a group is then obtained.
6- Prior to the computation of the score, every component of the score is normalized to its maximum value obtained during the 30 k-means implementations. The k option that achieves highest sum of scores is selected and, among its 10 implementations, the centre configuration that maximizes the score is chosen (Fig. 2j-l).

2.3.3.2. Refined classification of caveolar structures. To improve the initial classification of caveolar regions obtained with the scan approach using TEMCell-CNN, the specialized TEMCav-CNN model for classification of caveolar structures (single-pit, rosettes, and cavicles) is automatically applied to 148x148 nm^2 crops centred at individual caveolae centres found in the previous section (Fig. 2k, l). Because the definition of a rosette is a caveolae cluster, all caveolae coming from groups of two or more caveolae (k > 1) are classified as rosettes. A predefined, user-modifiable confidence parameter excludes predictions under a probability threshold, eliminating some erroneous caveolae predictions (Fig. 2m, arrowheads in Fig. 2l).

Since PM and LD surfaces were properly delimited from the pseudo-segmentation obtained with TEMCell-CNN model (section 2.3.2.2), information about caveolar distance to periphery can be exploited. Single-pit predictions farther than 150 nm from the PM are automatically deemed erroneous and reassigned to the second most likely class (Fig. 3a-c). The subtool is also able to calculate PM-LD distance through caveolar coordinates in an automated manner, which can be useful for further spatial caveolae analysis (Fig. 3b). All refinement and postprocessing steps are performed in the same run as cell pseudosegmentation and caveolae detection, without need of further user input.

3. Results

3.1. TEMCell-CNN correctly classifies most cellular structures

TEMCell-CNN model was trained to classify TEM image crops in 9 categories (LD, ECM, cytoplasm, mitochondria, ER, endosomes, and three caveolar structures: single-pits, rosettes, and cavicles) using 36,000 crop images including test, training and validation sets (Supp. Fig. 1c). Defining accuracy as the percentage of correctly classified instances, the test set reached a global accuracy of 83.84 %, with most of the confusion involving wrong caveolar classification (Fig. 3d). However, the network showed a high ability to discriminate between caveolar vs non-caveolar structures, reaching a 97.44 % caveolae/non-caveolae classification accuracy. Caveolae/non-caveolae classification accuracy was calculated by adding the number of caveolae classified as cavicle, rosette or single-pit, plus the number of non-caveolaer structures (LD, ECM, cytoplasm, ER, mitochondria or endosomes) that are classified as any non-caveolar class, and dividing this sum by the number of total instances. A complete list of evaluation metrics can be found in Supplementary Table 1.

Most classification errors occur among caveolar categories, achieving a 67,3% of classification accuracy (Fig. 3d). A possibility is that this confusion derives from the high number of categories

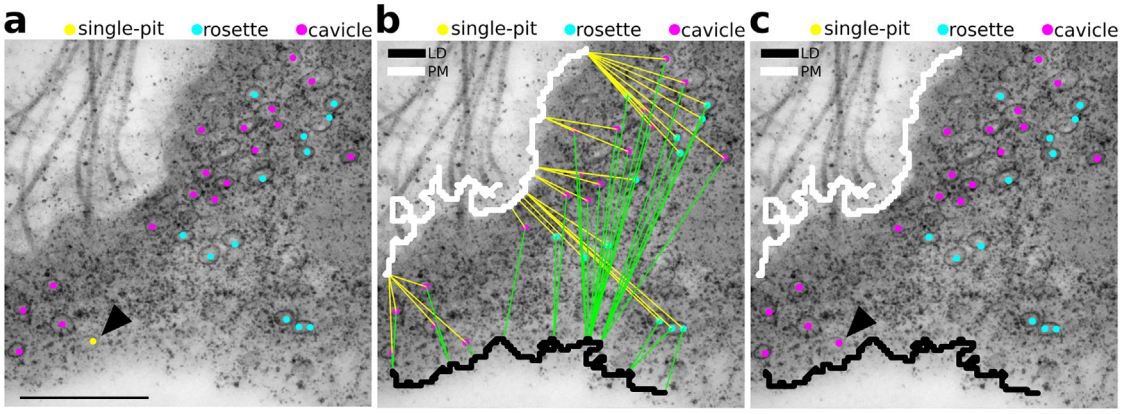

d

Real class

Predicted class	cavicle	rosette	single-pit	LD	ecm	cytop	ER	mitoc	endos
cavicle	0.702	0.216	0.132	0	0	0.016	0.004	0	0.006
rosette	0.172	0.62	0.144	0	0.002	0.024	0.01	0.002	0.004
single-pit	0.08	0.11	0.698	0	0	0.03	0.004	0	0.002
LD	0	0	0	0.988	0.056	0.002	0	0	0
ecm	0.002	0	0.004	0.012	0.87	0.048	0.004	0	0.008
cytop	0.028	0.032	0.02	0	0.06	0.832	0.018	0.008	0.004
ER	0.008	0.018	0.002	0	0.002	0.006	0.928	0.016	0.038
mitoc	0.002	0	0	0	0.002	0.028	0.008	0.972	0.002
endos	0.006	0.004	0	0	0.008	0.014	0.024	0.002	0.936

e

Real class

Predicted	cavicle	rosette	single-pit
cavicle	0.828	0.336	0.176
rosette	0.098	0.55	0.064
single-pit	0.074	0.114	0.76

f

	Human 1 t1	Human 1 t2	Human 2	Model
Single-pit	6	5	75	10
Rosette	516	534	407	577
Cavicle	397	478	450	348
Total	919	1017	932	935

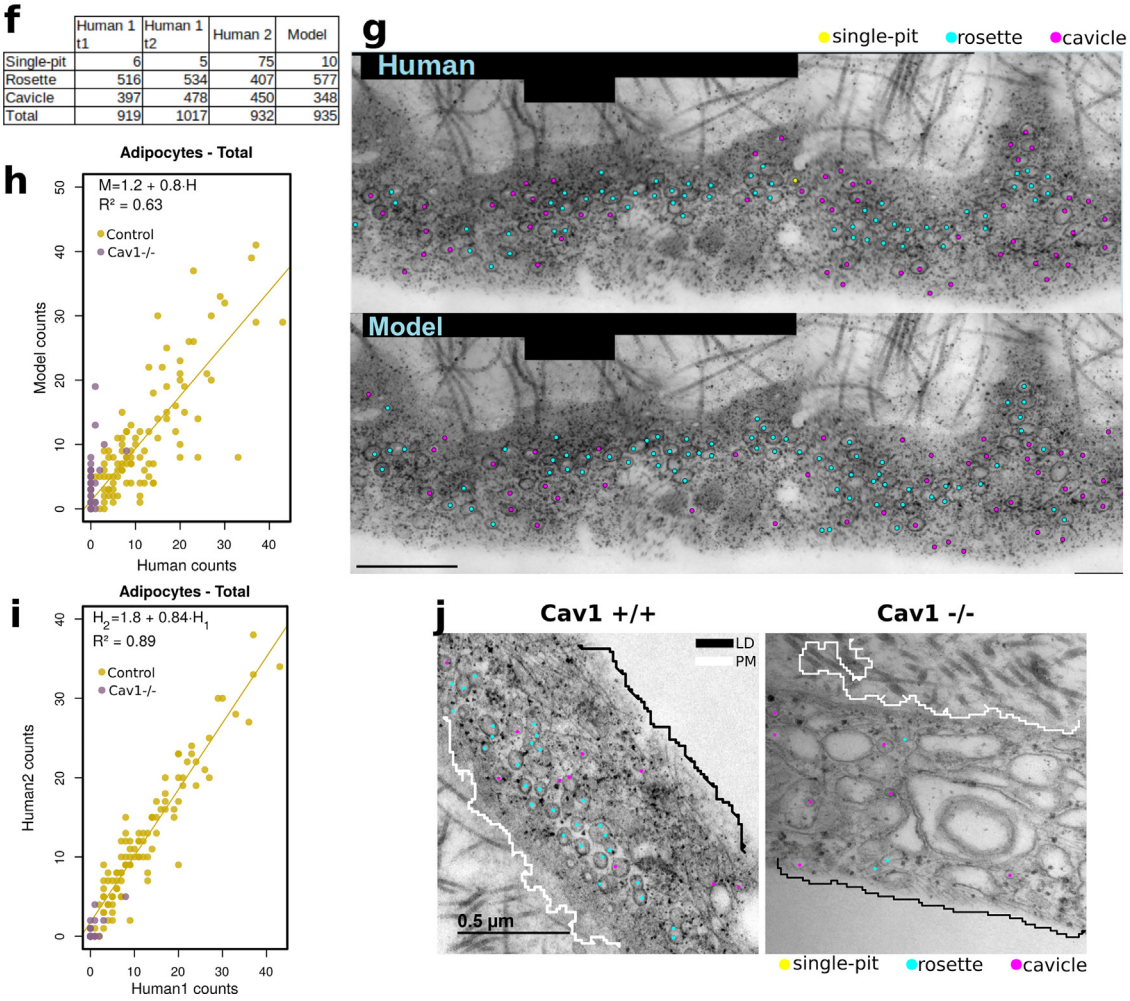

Fig. 3. Further caveolae classification refinement and tool validation in adipocytes. A: TEMCav-CNN predictions are sometimes obviously erroneous, finding some single-pit caveolae in regions distant from the PM. B: Since PM and LD are delimited, caveolar distance from these surfaces can be obtained. C: Single-pit predictions located far from the PM are reassigned to the second most probable caveolar type. D: Confusion matrix for the test set of TEMCell-CNN. E: Confusion matrix for the test set of TEMCav-CNN. F: Total caveolae counts for the whole adipocyte section on Fig. 1g. The table includes counts from one human (Human1) at two different time points (t1 and t2, where t2-t1 > 10 months) and a second human (Human2), as compared with the model. G: Representative results for the adipocyte section on Fig. 1h, showing comparable caveolae localization by Human1 and the model. H: Correlation of caveolae total counts provided by the model and a human expert in 100 independent image tiles from different cells or cellular locations for control (yellow) and 40 image tiles from caveolae-depleted cells (pink). I: Correlation of caveolae total counts provided by two different human experts. J: Final caveolae detection in Cav1+/+ (left) and Cav1-/- (right) adipocytes from mouse epididymal tissue. Scale bar: 0.5 µm.

included, and thus accuracy could be improved with a more specialized model. To test this possibility, we trained a second model exclusively on the three caveolar categories using the same data, TEMCav-CNN, reaching a slight improvement on test set accuracy of 71.27 % (Fig. 3e), but supporting the need of refinements and a specialized, automated downstream analysis of caveolar structures to improve their final classification. See Supp. Table 1 for a full evaluation of both models.

In order to achieve some explicability for the predictions our neural networks, we used Gradient-weighted Class Activation Mapping (Grad-CAM [36]) (Supp. Fig. 1d,e). This approach produces localization maps highlighting the regions of the image that are important for class prediction. Some patters can be recognized in Grad-CAM maps: for the case of single-pits, the four convolutional layers of TEMCell-CNN focus on caveolae membrane, particularly at the region of the neck and the surrounding flat membrane, while the vesicle interior produces negative output values, particularly in the fourth convolutional layer. In the case of rosettes, both caveolae membrane and inner regions appear highlighted, while in the case of cavicles, caveolae borders and surrounding areas produce the more positive values. LD crops show sparse highlights through the whole crop area and, for the rest of the categories, highlights coincide with relevant aspects of the image (collagen fibers for ECM, ribosomes for cytoplasm, cisternae borders for ER, mitochondrion double-membrane and endosome membrane). Some patterns are also observable in TEMCav-CNN Grad-CAM maps, which focus on neck regions for single pits and rosettes, as well as cavicle borders and surrounding areas.

3.2. Whole image scan with TEMCell-CNN provides consistent pseudo-segmentations

The TEMCell-CNN model performs classification of image crops, while our objective remains on the more complex spatial localization of caveolar and cell structures in full TEM images and large reconstructions of them. First, to transform classification labels into spatial data, the tool scans through the image using a sliding-window approach, extracting crops with a user-defined window size and displacement (Fig. 1c). Crops were then fed to the TEMCell-CNN model to obtain predictions. Because the network shows a higher than expected confusion among caveolar types, single-pit, rosette and cavicle predictions were merged in a single caveolae category for further processing and advanced reclassification using the TEMCav-CNN model. Model predictions of final 7 categories are assigned to the central coordinate of each crop, providing a pseudo-segmentation of cell regions (Fig. 1c).

The sliding window approach was successful, specially to differentiate between caveolar and non caveolar regions (Fig. 1d). We have obtained optimum results using a 70x70 pixel^2 sliding window size and 10 pixel displacement for 1024x1024 pixel^2 images of 1.478 nm pixel size (Supp. Fig. 2). These predefined parameters may need adjustment depending on expected caveolae size. A higher dimension for the sliding window may cause merging of different class-consistent caveolar groups, and thus complicate downstream cluster analysis and caveolar centre finding (Supp. Fig. 2). Higher values for sliding window displacement may lead to insufficient resolution for caveolar area delimitation, and lower values involve an increase in processing time with small benefit. Supp. Fig. 2 displays an example of results obtained with different set-ups for the sliding-window approach.

Initial predictions contained isolated areas of clearly erroneous patches that were corrected (Fig. 1c, d) after consistency-based reclassification. Coordinates of plasma membrane (PM, Cytoplasm-ECM contact regions) and LD surface (cytoplasm-LD contact regions) were detected and annotated automatically (Fig. 1-e-f). In large reconstructions of adipocyte sections, a final global classification refinement of PM and LD surfaces was applied by ensuring consistency in the set of TEM image tiles corresponding to the same cell (Fig. 1h-j). Detailed information about these corrections and refinements driven by the consistency of spatial context can be found in Materials and Methods section. Results (Fig. 1d) display good predictions of caveolar structures and accurate pseudo-segmentations of these specially challenging TEM images.

Consistent with the fact that caveolae image crops used for the training were centred in caveolae, caveolae prediction probabilities tended to be higher when the crop resulting from the sliding-window was centred at caveolae (Fig. 2i,k). On the contrary, prediction probability was lower and entropy higher at caveolae borders (Fig. 2k, Supp. Fig. 3a,b), indicating a higher uncertainty.

3.3. Improved detection of caveolar structures is comparable to experts in adipocytes

To improve results of classification into the three caveolar categories obtained with TEMCell-CNN and TEMCav-CNN models, additional automatic downstream analysis was developed to refine both detection of caveolar locations and their classification, by using information from the surrounding spatial context, increasing robustness and consistency of results.

First, grid-like coordinates of caveolar predictions obtained with TEMCell-CNN model were cleaned and grouped spatially, representing individual or clustered caveolae (Fig. 2a-f). Cluster analysis was performed in these class-consistent caveolar groups in order to locate caveolar central coordinates, using a score based on biological characteristics of caveolae that also select the correct number of cluster elements (caveolae) in each group (Fig. 2j-k). Additionally, pseudosegmentation for individual caveolae is obtained (Fig. 2l).

TEMCav-CNN model was used to classify these caveolar central coordinates (Fig. 2m) in the three categories (single-pit, cavicle, and rosette). To further increase accuracy in caveolae classification, contextual spatial information was again taken into account, reclassifying caveolar clusters to the rosette category, and using distance to PM to refine single-pit category assignations (Fig. 3a-c). The result is a set of coordinates representing central locations of caveolae, which can be used to quantify abundances for each caveolar category.

In a reconstructed section of a whole cell (Fig. 1f,g), the model provided total caveolae counts that were within the range of variability of different human observers (Fig. 3f), and successfully located caveolae centres, with a performance comparable to human manual caveolae localization (Fig. 3g). Despite the stochastic initiation of the k-means algorithm, we find consistent results in several runs of analysis of the same section, obtaining only minor variations in rosette counts (Supp. Table 2). Some discrepancy is expected between model and human counts, since TEM images are sometimes ambiguous and human observers also show some level of disagreement in caveolae classification (Supp. Fig. 3c). When run on image tiles from adipocytes that were independent from the training set, the model predicted caveolae numbers that were highly correlated to those obtained by human manual count (Fig. 3h), showing some dispersion that was expected, since there is also some level of discrepancy among two independent human observers (Fig. 3i). To further demonstrate the performance of the tool, images of Cav1-/- caveolae depleted cells were also evaluated. Contrary to human observers, the model predicted a small but positive amount of caveolae in Cav1-/- cells (Fig. 3h, i). This is probably caused by the presence of a high number of vesicles and organelles in the cytoplasm of caveolae depleted cells (Fig. 3j), in contrast with the highly uniform cytoplasm of the controls. Despite of this, the model was able to

find a drastic reduction in caveolae numbers in Cav1-/-, similar to human manual count (Fig. 3h, i). Regarding the performance of the model for caveolae classification, we obtained a low agreement between model and human, especially for single-pits, that are very often misclassified (Supp. Fig. 3d-f). A big disagreement can be found also for two different human observers, although in this case the class with the highest disagreement was rosettes (Supp. Fig. 3-g-i), likely due to image ambiguity, such as in the example in Supp. Fig. 3c. An example of disagreement between human and model single-pit localization is included in Supp. Fig. 3j-k. In this example, the model was able to properly localize caveolae, but most single-pits are misclassified as rosettes. This happens with all the single-pits that are in close vicinity to other single-pits, while the one that is more isolated at the right corner is properly classified. Indeed, we found other examples where the single-pit category is properly assigned when caveolae are sparser (Supp. Fig. 3l), probably indicating that the tool tends to classify caveolae as rosettes when they are tightly packed together. Other possible errors in caveolae classification may arise in cases of incorrect surface delimitation, that may lead to reclassification of single-pits when a long caveolae-PM distance is obtained (Supp. Fig. 3m). Another possible source of error is that unusual, elongated caveolae morphologies are predicted at lower probability, and thus are disregarded when increasing the confidence threshold (Supp. Fig. 3n).

3.4. The tool performs well in endothelial cells but provides poor results in human skin fibroblasts.

Regarding caveolae total counts, the performance of the tool in endothelial cells is similar to the performance in adipocytes (Fig. 4a). However, similarly to what we found for adipocytes, the performance is lower in the case of caveolae classification (Fig. 4 b-d). A known source of error is the occasional incorrect estimation of average caveolae area, which may lead to an incorrect estimation of the k parameter to calculate the number of caveolae contained in a cluster. If estimated average caveolae area is small, total caveolae counts can be overestimated (Fig. 4 e), even when caveolar area was perfectly segmented (Fig. 4f). Another source of error is the inability of the tool to detect the basement membrane, which is not present in the adipocytes for which it was designed. This impedes single pit localization at this membrane (Fig. 4e, g). However, the luminal PM is correctly delimited. Although the tool was designed to differentiate between PM and LD, a parameter indicating if the LD is expected can be modified so any cytoplasmic surface will be assigned as PM, thus avoiding unnecessary errors.

Despite known errors and the evident need to readjust the tool to the particularities of this cell type, several examples show a very promising performance (Fig. 4h-j).

Images of human skin fibroblasts showed a number of challenges that diminish the performance of the tool, but open new opportunities to understand and improve its applicability. These cells show a much lower spatial density of caveolae, and a higher proportion of single pits (Fig. 5). They also show no big LDs as opposed to adipocytes, and their ECM is less evident, often not even observable. To adapt the tool to this situation, we performed the following adjustments: 1) we eliminated the steps needed to differentiate between PM and LD, as in the case of endothelial cells and, thus, all cytoplasmic surfaces were assigned to PM; 2) caveolae belonging to a cluster were only reassigned to the rosette type if they were not classified as single-pits by TEMCav-CNN.

Another limitation that we found is that these cells have a high cytoplasmic content and a high proportion of organelles. This is a source for error that diminishes the performance of the tool, even when caveolae were almost perfectly localized (Fig. 5a). In this case, a high number of caveolar predictions are assigned to ER membranes and intracellular membranes, indicating that the tool likely needs retraining with image crops from the cytoplasm of these cells. This did not happen always, and most image tiles show no incorrect predictions even in the presence of large amounts of ER and nucleus (Fig. 5b).

The tool also misses a significant amount of caveolae, and some are misclassified as ER (Fig. 5 c,d). This reaffirms the need for specific retraining (or transfer learning) for this cell line. Despite the evident errors, the tool is able to see a slight reduction in caveolae numbers as a result of 10 min of hypoosmotic treatment (1/10 dilution of DMEM), as shown in Fig. 5 e,f, Fig. 6a. This difference was particular to the cavicle type (Fig. 6a) which is a clear disagreement with the results obtained by human experts (Fig. 6b), which demonstrate that the rosette class is the most affected by the hypoosmotic shock [31]. This demonstrates again that the tool performance is more reliable for caveolae localization and counting than for caveolae classification. Total human and tool counts are correlated, but the underestimation of caveolae numbers by the tool is evident, as well as some instances of erroneously high counts corresponding to false positives throughout cytoplasmic organelles (Fig. 6c, Fig. 5a). The discrepancy is also high between tool and human expert for the different caveolae classes (Fig. 6c). Thus, the tool is not reliable at this step for caveolae analysis in human skin fibroblasts, and needs further adjustment and retraining for this cell line.

4. Discussion

TEM provides complicated images that are often analysed manually, involving a considerable amount of repetitive and tedious work, which limits throughput and reproducibility. Thus, there is a need for new approaches on automated image analysis centred on TEM, which would be relevant for the study of nanoscopic cellular structures such as caveolae.

Here, we generated a training set with numerous caveolae images and trained a convolutional neural network that can differentiate them from different cytosolic structures present in adipocytes, thus potentially replacing the tedious manual work that is currently needed to locate caveolae in TEM images. As a result, we provide a new tool for the automated quantification of caveolae and cytoplasmic boundaries, with possible applications for the study of plasma membrane mechanical dynamics.

The tool is designed to work automatically, and it is able to estimate optimal sliding window parameters based on reported caveolae size from the literature and image scale from metadata (if available). Only minimal user input is needed when the use of non-default parameters is preferable. However, some optimization is recommended in a subset of images to ensure acceptable performance. The user can specify the image scale and tune sliding window parameters and/or expected caveolae size ranges, set a confidence threshold (minimum caveolae prediction probability required), or modify the estimated average caveolae area for k estimation during cluster analysis. The user can also specify if a LD droplet is expected, if they want caveolae distances to PM and LD calculated, or if they want clustered caveolae to be reassigned as rosettes despite TEMCav-CNN predictions. A full manual with troubleshooting suggestions is available at https://github.com/MariaAboy/DLCaveolae.

We acknowledge that this tool may present several limitations. First of all, this tool is designed for unlabelled TEM images, and we don't expect it to perform well in other EM techniques. Importantly, caveolae identification and classification in unlabelled TEM images is a challenging and subjective task with significant variation among human observers. Immunogold labelling of caveolar components could increase the certainty of caveolae classifica-

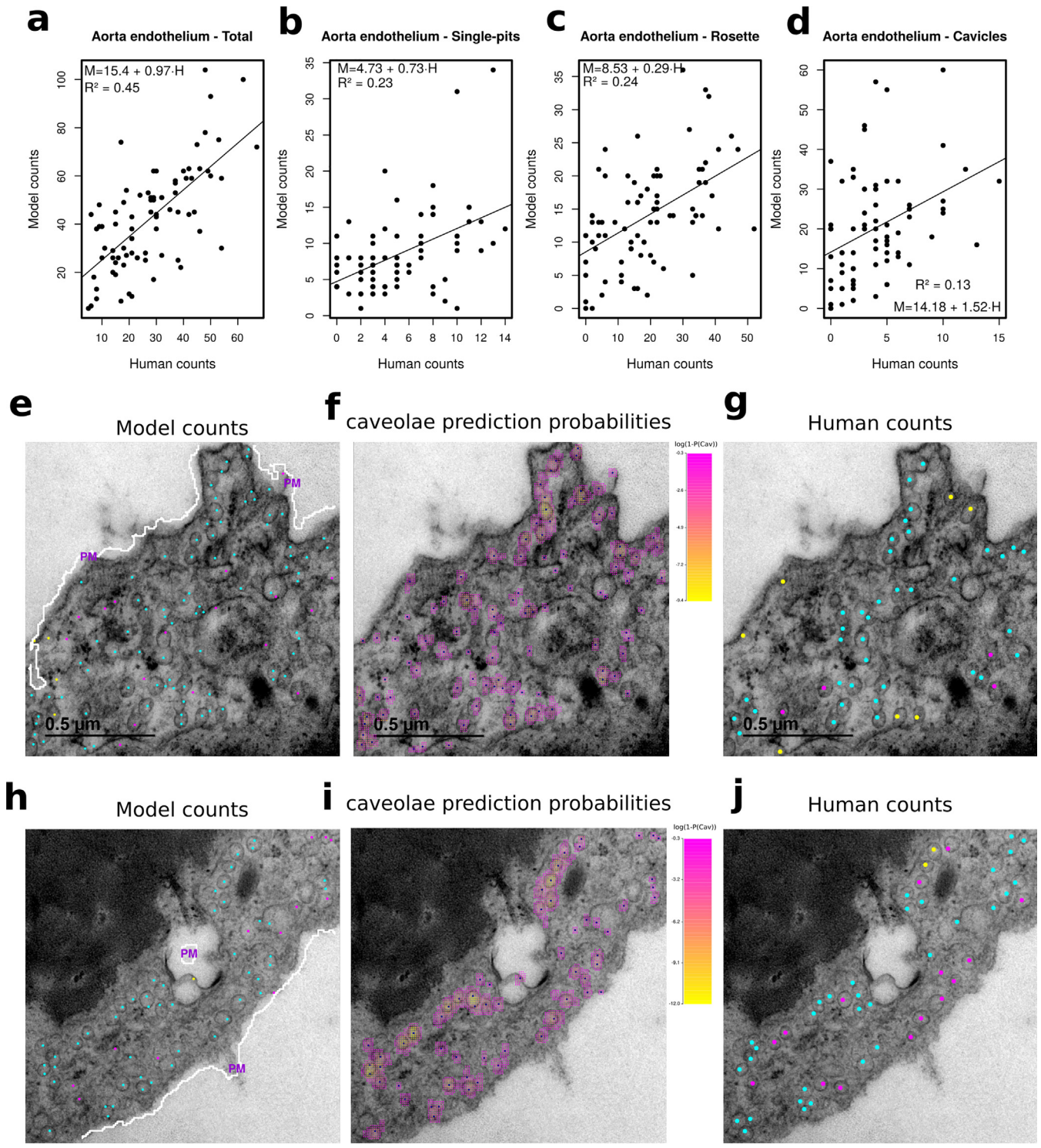

Fig. 4. Tool performance in endothelial cells from mouse aorta. A: Correlation of caveolae total counts provided by the model and a human expert. B: Correlation of single-pit counts provided by the model and a human expert. C: Correlation of rosette counts provided by the model and a human expert. D: Correlation of cavicle counts provided by the model and a human expert. E: Example of caveolae localization provided by the model, showing an excess of caveolae coordinates. F: Example of correct caveolae area pseudo-segmentation by the tool. G: Caveolae localization by a human expert in the same image. H: Example of successful caveolae localization provided by the model. I: Correct pseudosegmentation of caveolae regions by the tool in the same image. J: Caveolae localization by a human expert in the same image.

tion, but would in turn impact sample preservation and render images with lower contrast. Unlabelled, conventional TEM thus provides the highest resolution for caveolae structures and is commonly used for caveolar structure classification.

Caveolae TEM images can sometimes be ambiguous and this tool will be affected by all the limitations of TEM imaging. For example, cavicles may seem detached from the cell surface in 2D sections, but in fact be connected with other caveolae or with the cell surface at another level. Indeed, the number of true cavicles may be significantly lower than we could initially assume by observing 2D sections, and most of them could actually be single-pits or rosettes whose connections do not appear in the sec-

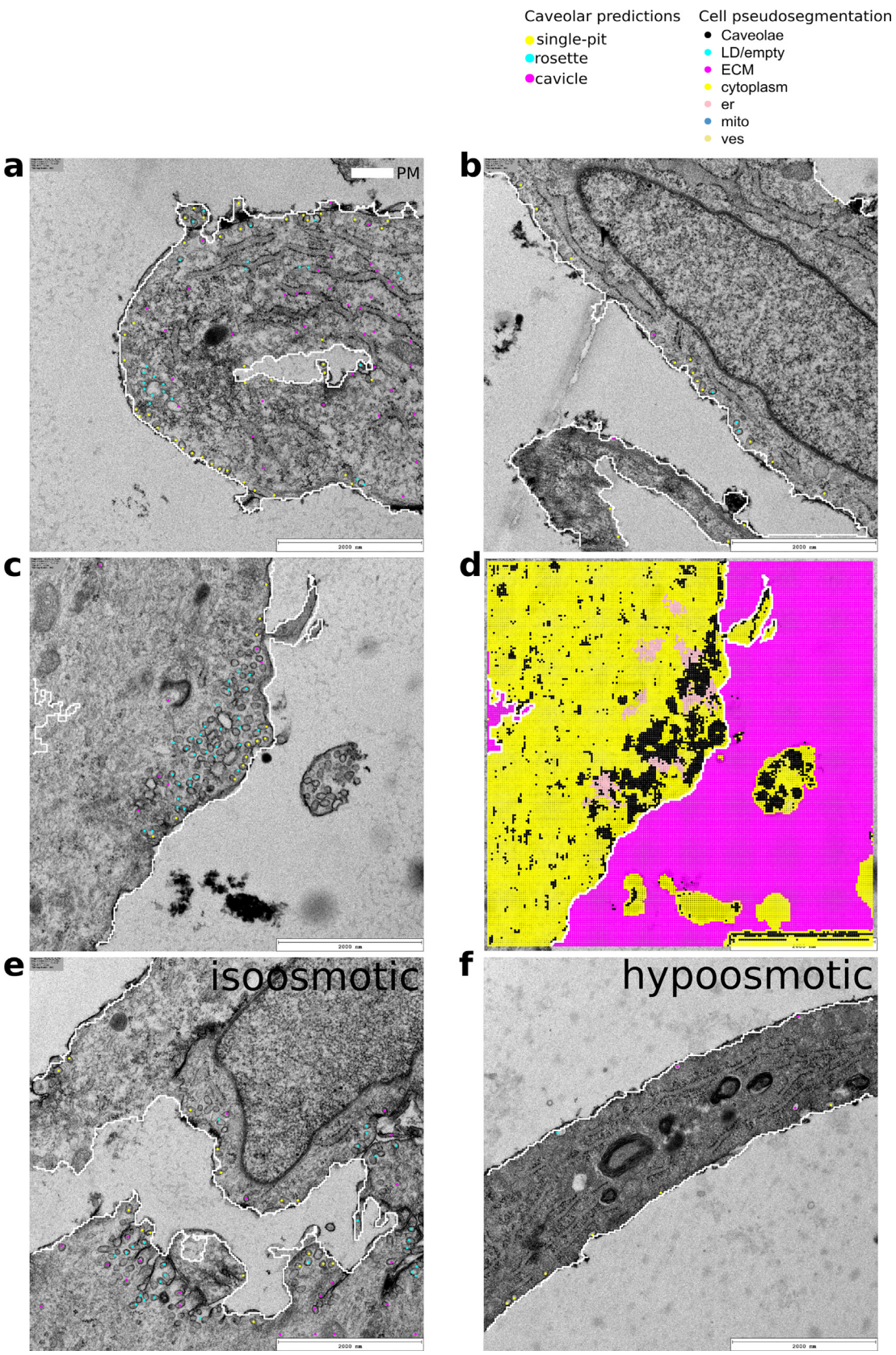

Fig. 5. Tool performance in human skin fibroblasts. A: Evidence of false positive caveolae localization in ER areas. B: Example of correct caveolae localization with no evident false positive localization. C: Example of insufficient caveolae localization, with evident false negative instances. D: Example of incorrect detection of caveolae areas as ER in the same image as in C. E: Representative example of caveolae detection in a isosmotic control. F: Representative example of caveolae detection in a fibroblasts treated with hypoosmotic media.

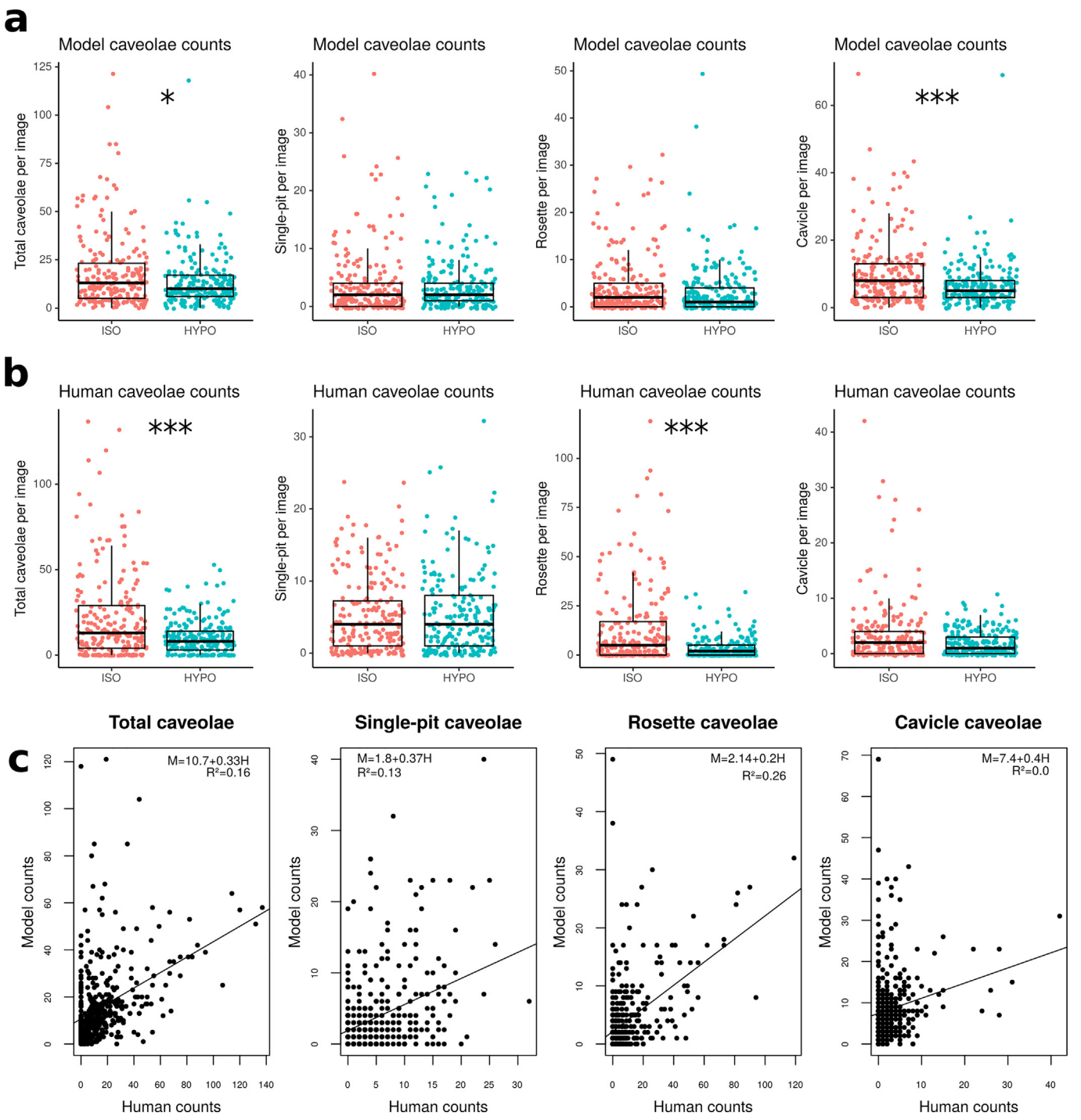

Fig. 6. Quantification of tool performance in human skin fibroblasts. A: Model counts of total caveolae and different caveolae classes in isosmotic and hypoosmotic conditions. B: Human expert counts of total caveolae and different caveolae classes in isosmotic and hypoosmotic conditions. C: Correlation of model and human expert counts for total caveolae and different caveolae classes.

tion, as it has been shown previously by other authors [31,32,37,38].

Important to note also is that the cluster analysis approach to find caveolae centres can have some limitations. When there are several caveolae clustered together, there is chance for several sources of error; for example, caveolae area is assumed to be constant in the image, but some variability exists. A prediction group where some caveolae are smaller than estimated can result in some caveolae being missed because the algorithm seeks for a number of clusters that is smaller than the real caveolae number. The same way, if a prediction group is composed by caveolae that are bigger than average, it can result in overestimation of caveolae numbers and some caveolae being located twice. Another limitation of this approach is that, if caveolae cluster centres are not properly localized because the solution found by the k-means is suboptimal, then the crop that is obtained to reclassify caveolae may be not centred and thus the prediction probability may be low. Also, caveolae classification may be impaired if, for example, the uncentered crop does not include existing caveolae necks or connections.

There is also a possible downside to classifying all clustered caveolae as rosettes. This approach compensates the tendency of TEMCav-CNN to erroneously classify a significant proportion of rosettes as cavicles (Fig. 3e), but it may lead to the wrong classification of individual single pits that are too close to each other to be found separately (Supp. Fig. 3j). This effect will be more important the bigger the sliding window size. Also, by design of the training set, all clustered caveolae are assigned to the rosette category, and the tool is unable to differentiate other caveolar clustered structures or elongated tubules.

Also of note, the approach we have presented demands a high spatial consistency to consider caveolae predictions as reliable. Discarding isolated caveolae predictions as in Fig. 2a-e requires that a caveolae is detected several consecutive times to be considered for downstream analysis. This is required to ensure that the tool is robust and the false positives are kept to a minimum, but can lead to some undetected caveolae.

Another important limitation is that this tool has been optimized solely in TEM images from adipocytes. Although we showed a satisfactory performance also in endothelial cells, further testing is needed to assess applicability to different cell types, which may need retraining, especially in the presence of staining artefacts or cellular structures that are uncommon in adipocytes and have not been included in the training. This is the case of skin fibroblasts, where the tool could detect a reduction in caveolae counts as a result of hypoosmotic treatment, but would need retraining and significant adjustments to provide better, more reliable results. The tool is also unable to recognize nuclei, and mostly classifies nuclear regions as cytoplasm or mitochondria (Supp. Fig. 4). Also, the tool provides caveolae counts per tile, and cell surface reconstruction has been optimized for images with a single adipocyte (Fig. 1h-j). Future work will focus on providing caveolae counts per cell within each tile, and exploring cell surface reconstruction in sections with several adipocytes.

The tool was also optimized in images with a pixel size of 1.478 nm, and, although it is able to provide a recommended sliding window size and displacement depending on the scale, some adjustment of sliding window parameters may be needed in the case of caveolae with diameters outside the 50–80 nm range. Importantly, in the case of caveolae-depleted adipocytes, the tool finds a significant amount of erroneous caveolae. This is probably due to the particular structure of Cav1$^{-/-}$ cytoplasm, that shows an increased density of vesicles and organelles as compared to control cells. Thus, the tool may perform badly on cells that show a high density of non-caveolar vesicles, and will likely be unable to differentiate between caveolae and other non-caveolar vesicles that have not been included in the training. Because the tool has not been trained in non-caveolar vesicles like clathrin coated pits, we don't expect it to be able to differentiate them from caveolae, especially in cases when their size is similar. This could also lead to false positive caveolae detections.

Another limitation of the tool is the slow sliding-window approach, since the R script is unable to automatically process several images in parallel. Processing of a single 1024x1024 pixel^2 image with a window displacement of 10 pixels in a i7 2.7–3.6 GHz processor can take up to 12 min, although several images can be run in parallel in different R sessions. Decreasing the sliding window parameter leads to a quadratic increase in the number of predictions, thus leading to an equivalent increase in processing time.

In conclusion, we have presented a new tool for automated caveolae detection in TEM images, aiming to facilitate the detailed study of PM ultrastructure. This work also opens new possibilities for the automated recognition of different cellular structures, including caveolae, ER, mitochondria and endosomes.

Declaration of Competing Interest

The authors declare that they have no known competing financial interests or personal relationships that could have appeared to influence the work reported in this paper.

Acknowledgements

We thank Dr Asier Echarri and Dr Fidel Lolo for providing fibroblast and endothelial cell images to validate the tool. We thank Juan José Lazcano and Elisabet Daniel for mouse colony management, and Francisco Urbano and Covadonga Díaz from Universidad Autónoma de Madrid for TEM technical support; This study was supported by grants from the Spanish Ministry of Science and Innovation (MICIIN)/Agencia Estatal de Investigación (AEI)/European Regional Development Fund (ARDF/FEDER) "A way to make Europe" (PDC2021-121572-100, IGP-SO grant MINSEV1512-07-2016, and PID2020-118658RB-I00), Comunidad Autónoma de Madrid (Tec4Bio-CM, S2018/NMT¬4443), Fundació La Marató de TV3 (201936-30-31), Asociación Española Contra el Cáncer (PROYE20089DELP), and Fundación Obra Social La Caixa (AtheroConvergence, HR20-00075), all to M.A.d.P. M.C.M.A-P. was sponsored by a la Caixa-Severo Ochoa international doctoral fellowship, 2015 call. V.J-J. was ECR trainee of a Horizon 2020 MSCA-ITN (BIOPOL, 641639), of which M.A.d.P. was co-awardee. L.S.A. was sponsored by a FPU doctoral fellowship from the Ministerio de Universidades (FPU18/05394). The CNIC is supported by the Instituto de Salud Carlos III (ISCIII), the Ministerio de Ciencia e Innovación (MICIIN) and the Pro CNIC Foundation, and is a Severo Ochoa Center of Excellence (grant CEX2020-001041-S funded by MICIN/AEI/10.13039/501100011033).

Author contributions

M.C.M.A-P. conceived the project, generated the majority of the training set images and coded the algorithm. D.J.C. contributed to neural network architecture optimization and to cluster analysis for caveolar central coordinate detection. M.C.M.A-P. and D.J.C. wrote the manuscript with input from all the authors. S.T. and D. P. contributed to the generation of the training set images. L.S.A. contributed to the annotation of new images used for the validation of the tool. V.J-J. provided ideas and advice for cytoplasm surface reconstruction and edited the manuscript. F.S.C. and M.A.d.P. supervised procedures and experimental design, and M.A.d.P. provided funding.

Data and code availability

R code and models are available at github.com/MariaAboy/DLCaveolae. Annotated training images are available upon request.

Appendix A. Supplementary data

Supplementary data to this article can be found online at https://doi.org/10.1016/j.csbj.2022.11.062.

References

[1] Farquhar MG, Palade GE. Junctional complexes in various epithelia. J Cell Biol 1963;17:375–412. https://doi.org/10.1083/jcb.17.2.375.
[2] Yamada K. Some Aspects of the Fine Structure of the Gall Bladder Epithelium of the Mouse. Okajimas Folia Anat Jpn 1968;45:11–9. https://doi.org/10.2535/ofaj1936.45.1_11.
[3] Cheng JPX, Mendoza-Topaz C, Howard G, Chadwick J, Shvets E, Cowburn AS, et al. Caveolae protect endothelial cells from membrane rupture during increased cardiac output. J Cell Biol 2015;211:53–61. https://doi.org/10.1083/jcb.201504042.

[4] Dewulf M, Köster DV, Sinha B, Viaris de Lesegno C, Chambon V, Bigot A, et al. Dystrophy-associated caveolin-3 mutations reveal that caveolae couple IL6/STAT3 signaling with mechanosensing in human muscle cells. Nat Commun 2019:10. https://doi.org/10.1038/s41467-019-09405-5.
[5] Garcia J, Bagwell J, Njaine B, Norman J, Levic DS, Wopat S, et al. Sheath Cell Invasion and Trans-differentiation Repair Mechanical Damage Caused by Loss of Caveolae in the Zebrafish Notochord. Curr Biol 2017;27:1982–1989.e3. https://doi.org/10.1016/j.cub.2017.05.035.
[6] Lim YW, Lo HP, Ferguson C, Martel N, Giacomotto J, Gomez GA, et al. Caveolae Protect Notochord Cells against Catastrophic Mechanical Failure during Development. Curr Biol 2017;27:1968–1981.e7. https://doi.org/10.1016/j.cub.2017.05.067.
[7] Lo HP, Nixon SJ, Hall TE, Cowling BS, Ferguson C, Morgan GP, et al. The caveolin-Cavin system plays a conserved and critical role in mechanoprotection of skeletal muscle. J Cell Biol 2015;210:833–49. https://doi.org/10.1083/jcb.201501046.
[8] Sinha B, Köster D, Ruez R, Gonnord P, Bastiani M, Abankwa D, et al. Cells respond to mechanical stress by rapid disassembly of caveolae. Cell 2011;144:402–13. https://doi.org/10.1016/j.cell.2010.12.031.
[9] Cao H, Alston L, Ruschman J, Hegele R, a.. Heterozygous CAV1 frameshift mutations (MIM 601047) in patients with atypical partial lipodystrophy and hypertriglyceridemia. Lipids Health Dis 2008;7:3. https://doi.org/10.1186/1476-511X-7-3.
[10] Garg A, Kircher M, del Campo M, Amato RS, Agarwal AK. Whole exome sequencing identifies de novo heterozygous CAV1 mutations associated with a novel neonatal onset lipodystrophy syndrome. Am J Med Genet A 2015;167:1796–806. https://doi.org/10.1002/ajmg.a.37115.
[11] Kim CA, Delépine M, Boutet E, el Mourabit H, le Lay S, Meier M, et al. Association of a homozygous nonsense caveolin-1 mutation with berardinelli-seip congenital lipodystrophy. J Clin Endocrinol Metab 2008;93:1129–34. https://doi.org/10.1210/jc.2007-1328.
[12] van der Pol RJ, Benninga MA, Magré J, van Maldergem L, Rotteveel J, van der Knaap MS, et al. Berardinelli-Seip syndrome and achalasia: a shared pathomechanism? Eur J Pediatr 2015;174:975–80. https://doi.org/10.1007/s00431-015-2556-y.
[13] Schrauwen I, Szelinger S, Siniard AL, Kurdoglu A, Corneveaux JJ, Malenica I, et al. A frame-shift mutation in CAV1 is associated with a severe neonatal progeroid and lipodystrophy syndrome. PLoS One 2015:10. https://doi.org/10.1371/journal.pone.0131797.
[14] Lee H, Park DS, Razani B, Russell RG, Pestell RG, Lisanti MP. Caveolin-1 mutations (P132L and null) and the pathogenesis of breast cancer: Caveolin-1 (P132L) behaves in a dominant-negative manner and caveolin-1 (-/-) null mice show mammary epithelial cell hyperplasia. Am J Pathol 2002;161:1357–69. https://doi.org/10.1016/S0002-9440(10)64412-4.
[15] Ardissone A, Bragato C, Caffi L, Blasevich F, Maestrini S, Bianchi ML, et al. Novel PTRF mutation in a child with mild myopathy and very mild congenital lipodystrophy. BMC Med Genet 2013;14:1–5. https://doi.org/10.1186/1471-2350-14-89.
[16] Hayashi YK, Matsuda C, Ogawa M, Goto K, Tominaga K, Mitsuhashi S, et al. Human PTRF mutations cause secondary deficiency of caveolins resulting in muscular dystrophy with generalized lipodystrophy. J Clin Investig 2009;119:2623–33. https://doi.org/10.1172/JCI38660.
[17] Murakami N, Hayashi YK, Oto Y, Shiraishi M, Itabashi H, Kudo K, et al. Congenital generalized lipodystrophy type 4 with muscular dystrophy: Clinical and pathological manifestations in early childhood. Neuromuscul Disord 2013;23:441–4. https://doi.org/10.1016/j.nmd.2013.02.005.
[18] Rajab A, Straub V, McCann LJ, Seelow D, Varon R, Barresi R, et al. Fatal cardiac arrhythmia and long-QT syndrome in a new form of congenital generalized lipodystrophy with muscle rippling (CGL4) due to PTRF-CAVIN mutations. PLoS Genet 2010;6:e1000874.
[19] Shastry S, Delgado MR, Dirik E, Turkmen M, Agarwal AK, Garg A. Congenital generalized lipodystrophy, type 4 (CGL4) associated with myopathy due to novel PTRF mutations. Am J Med Genet A 2010;152:2245–53. https://doi.org/10.1002/ajmg.a.33578.
[20] Jelani M, Ahmed S, Almramhi MM, Mohamoud HSA, Bakur K, Anshasi W, et al. Novel nonsense mutation in the PTRF gene underlies congenital generalized lipodystrophy in a consanguineous Saudi family. Eur J Med Genet 2015;58:216–21. https://doi.org/10.1016/j.ejmg.2015.02.002.
[21] Akinci G, Topaloglu H, Akinci B, Onay H, Karadeniz C, Ergul Y, et al. Spectrum of clinical manifestations in two young Turkish patients with congenital generalized lipodystrophy type 4. Eur J Med Genet 2016;59:320–4. https://doi.org/10.1016/j.ejmg.2016.05.001.
[22] Güneş N, Kutlu T, Tekant GT, Eroğlu AG, Üstündağ NÇ, Öztürk B, et al. Congenital generalized lipodystrophy: The evaluation of clinical follow-up findings in a series of five patients with type 1 and two patients with type 4. Eur J Med Genet 2019;63:2–7. https://doi.org/10.1016/j.ejmg.2019.103819.
[23] Patni N, Vuitch F, Garg A. Postmortem Findings in a Young Man With Congenital Generalized Lipodystrophy, Type 4 Due to *CAVIN1* Mutations. J Clin Endocrinol Metab 2019;104:957–60. https://doi.org/10.1210/jc.2018-01331.
[24] Wong TH, Khater IM, Joshi B, Shahsavari M, Hamarneh G, Nabi IR. Single molecule network analysis identifies structural changes to caveolae and scaffolds due to mutation of the caveolin-1 scaffolding domain. Scientific Reports 2021 11:1. 2021;11: 1–14. doi:10.1038/s41598-021-86770-6.
[25] Khater IM, Liu Q, Chou KC, Hamarneh G, Nabi IR. Super-resolution modularity analysis shows polyhedral caveolin-1 oligomers combine to form scaffolds and caveolae. Scientific Reports 2019 9:1. 2019;9: 1–10. doi:10.1038/s41598-019-46174-z.
[26] Khater IM, Meng F, Wong TH, Nabi IR, Hamarneh G. Super Resolution Network Analysis Defines the Molecular Architecture of Caveolae and Caveolin-1 Scaffolds. Scientific Reports 2018 8:1. 2018;8: 1–15. doi:10.1038/s41598-018-27216-4.
[27] Yang L, Scarlata S. Super-resolution Visualization of Caveola Deformation in Response to Osmotic Stress. J Biol Chem 2017;292:3779–88. https://doi.org/10.1074/JBC.M116.768499.
[28] Gabor KA, Stevens CR, Pietraszewski MJ, Gould TJ, Shim J, Yoder JA, et al. Super Resolution Microscopy Reveals that Caveolin-1 Is Required for Spatial Organization of CRFB1 and Subsequent Antiviral Signaling in Zebrafish. PLoS One 2013;8:e68759.
[29] Echarri A, del Pozo MA. Caveolae - mechanosensitive membrane invaginations linked to actin filaments. J Cell Sci 2015;128:2747–58. https://doi.org/10.1242/jcs.153940.
[30] Echarri A, Muriel O, Pavón DM, Azegrouz H, Escolar F, Terrón MC, et al. Caveolar domain organization and trafficking is regulated by Abl kinases and mDia1. J Cell Sci 2012;125:3097–113. https://doi.org/10.1242/jcs.090134.
[31] Echarri A, Pavón DM, Sánchez S, García-García M, Calvo E, Huerta-López C, et al. An Abl-FBP17 mechanosensing system couples local plasma membrane curvature and stress fiber remodeling during mechanoadaptation. Nat Commun 2019:10. https://doi.org/10.1038/s41467-019-13782-2.
[32] Golani G, Ariotti N, Parton RG, Kozlov MM. Membrane Curvature and Tension Control the Formation and Collapse of Caveolar Superstructures. Dev Cell 2019;48:523–538.e4. https://doi.org/10.1016/j.devcel.2018.12.005.
[33] del Pozo MA, Balasubramanian N, Alderson NB, Kiosses WB, Grande-García A, Anderson RGW, et al. Phospho-caveolin-1 mediates integrin-regulated membrane domain internalization. Nat Cell Biol 2005;7:901–8. https://doi.org/10.1038/ncb1293.
[34] Schindelin J, Arganda-Carreras I, Frise E, Kaynig V, Longair M, Pietzsch T, et al. Fiji: An open-source platform for biological-image analysis. Nature Methods. Nature Publishing Group; 2012. pp. 676–682. doi:10.1038/nmeth.2019.
[35] Kurt De Vos. Cell Counter. University of Sheffield; 2001. Available: https://imagej.nih.gov/ij/plugins/cell-counter.html.
[36] Selvaraju RR, Cogswell M, Das A, Vedantam R, Parikh D, Batra D. Grad-CAM: Visual Explanations from Deep Networks via Gradient-Based Localization. Int J Comput Vis 2020;128:336–59. https://doi.org/10.1007/S11263-019-01228-7/FIGURES/21.
[37] Bundgaard M, Hagman P, Crone C. The three-dimensional organization of plasmalemmal vesicular profiles in the endothelium of rat heart capillaries. Microvasc Res 1983;25:358–68. https://doi.org/10.1016/0026-2862(83)90025-0.
[38] Bundgaard M, Frokjaer-Jensen J, Crone C. Endothelial plasmalemmal vesicles as elements in a system of branching invaginations from the cell surface. Proc Natl Acad Sci U S A 1979;76:6439–42. https://doi.org/10.1073/pnas.76.12.6439.